

## Prediction of phonon-mediated superconductivity in borophene

Miao Gao,<sup>1,\*</sup> Qi-Zhi Li,<sup>1</sup> Xun-Wang Yan,<sup>2</sup> and Jun Wang<sup>1</sup>

<sup>1</sup>*Department of Microelectronics Science and Engineering, Faculty of Science, Ningbo University, Zhejiang 315211, People's Republic of China*

<sup>2</sup>*School of Physics and Electrical Engineering, Anyang Normal University, Henan 455000, People's Republic of China*

(Received 10 October 2016; published 10 January 2017)

Superconductivity in two-dimensional compounds is widely studied, not only because of its application in constructing nano-superconducting devices, but also for general scientific interest. Very recently, borophene (a two-dimensional boron sheet) has been successfully grown on the Ag(111) surface, through direct evaporation of a pure boron source. The experiment unveiled two types of borophene structures, namely  $\beta_{12}$  and  $\chi_3$ . Herein, we employed density-functional first-principles calculations to investigate the electron-phonon coupling and superconductivity in both structures of borophene. The band structures of  $\beta_{12}$  and  $\chi_3$  borophenes exhibit inherent metallicity. We found that electron-phonon coupling constants in the two compounds are larger than that in MgB<sub>2</sub>. The superconducting transition temperatures were determined to be 18.7 K and 24.7 K through the McMillian-Allen-Dynes formula. These temperatures are much higher than the theoretically predicted 8.1 K and experimentally observed 7.4 K superconductivity in graphene. Our findings will enrich nano-superconducting device applications and boron-related materials science.

DOI: [10.1103/PhysRevB.95.024505](https://doi.org/10.1103/PhysRevB.95.024505)

### I. INTRODUCTION

The discovery of graphene provides a fascinating playground for nanoscale device applications in the future [1]. This has triggered a surge of interest in the synthesis and investigation of two-dimensional (2D) compounds, such as silicene [2–4], germanene [5–7], transition-metal dichalcogenides [8–10], and phosphorene [11–13]. Borophene is another important 2D material which is also expected to act as a new functional compound or a precursor to construct boron nanotubes [14]. The 2D triangular lattice, with a buckling arrangement of boron atoms, is a metastable structure of the boron sheet. Theoretical studies suggested a set of more stable freestanding boron sheets by introducing some vacancy sites in the triangular lattice. The predicted boron sheets take either planar or buckled geometries, depending on the configurations of vacancies [15–19].

Very recently, the monolayer boron sheet has been successfully grown on the Ag(111) surface under ultrahigh vacuum [20,21], following the suggestion given by the first-principles simulation [22]. The scanning tunneling microscopy images obtained in experiment revealed two distinct phases of the boron sheet for different temperatures of the substrate. One is a striped phase; the other is a homogeneous phase. Mannix and co-workers suggested the striped phase should be a buckled triangular lattice without vacancy [20]. However, Feng *et al.* attributed the striped phase to a  $\beta_{12}$  model of the boron sheet with vacancies [21]. More importantly, the computed band structure based on a  $\beta_{12}$  model of the boron sheet with vacancies [see Fig. 1(a)] is in excellent agreement with the observed angle-resolved photoelectron spectroscopy [23]. A calculation combining the cluster expansion method with density-functional theory (DFT) found that the ground-state structure of the boron sheet on the Ag(111) surface is  $\beta_{12}$  [24]. Another simulation of the nucleation of boron on the Ag(111)

surface again prefers the  $\beta_{12}$  model [25]. On the other hand, the homogeneous phase of the boron sheet corresponds to the  $\chi_3$  structure [see Fig. 1(b)] [21]. Hereafter, we named these two boron sheets  $\beta_{12}$  borophene and  $\chi_3$  borophene, respectively.

One important application of 2D compounds is driving them to superconducting states to manufacture nano-superconducting quantum interference devices and nano-superconducting transistors [26,27]. The possibility of inducing superconductivity in graphene was explored by depositing metal atoms on it. The superconducting state in metal-coated graphene was first discussed through a plasmon-mediated mechanism in 2007 [28]. Subsequent DFT calculations suggested that superconducting transition temperatures ( $T_c$ ) are equal to 8.1 K for monolayer LiC<sub>6</sub>, and 1.4 K for monolayer CaC<sub>6</sub> [29]. Lately, superconductivity at 7.4 K in Li-intercalated few-layer graphene [30] and 6 K in Ca-decorated graphene [31] has been realized in experiment. Similar calculations were also carried out for silicene and phosphorene. The  $T_c$ s were found to be about 15.5 K and 12.2 K for electron-doped silicene and phosphorene under certain tensile strain [32–34]. It is noteworthy that graphene, silicene, and phosphorene are either semimetal or semiconductor with vanished density of states at the Fermi level. A prerequisite to induce superconductivity in these compounds is to introduce charge carriers by doping.

Distinct from the above semimetals or semiconductor,  $\beta_{12}$  and  $\chi_3$  borophenes are inherently metallic [20,21]. So superconductivity in borophenes is expected to be an important and interesting issue and deserves to be investigated. Herein, we chose  $\beta_{12}$  and  $\chi_3$  borophenes as two potential candidates to investigate their electron-phonon coupling (EPC) properties and possible superconductivity, based on the first-principles calculations and Eliashberg equations. We found that the bond-stretching  $A_g$  mode strongly couples with electrons in  $\beta_{12}$  borophene. In  $\chi_3$  borophene, several in-plane phonon modes have large contributions to EPC, especially the  $B_{1g}$  mode at the  $\Gamma$  point. To accurately determine the EPC constants, we employed the recently developed Wannier interpolation technique, which has been implemented in the EPW code (see

\*gaomiao@nbu.edu.cn

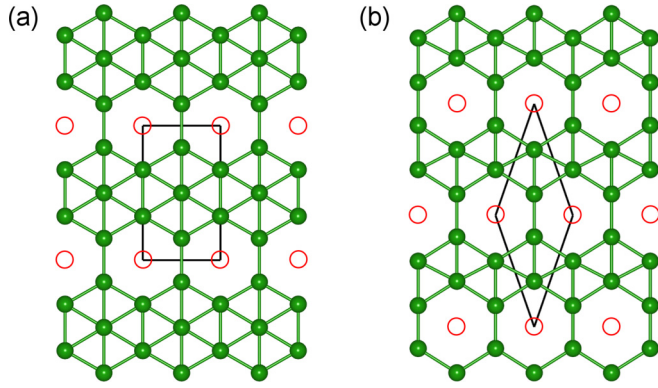


FIG. 1. Top views of borophenes. (a)  $\beta_{12}$  borophene. (b)  $\chi_3$  borophene. The green balls and red hollow circles represent the boron atoms and vacancy sites, respectively. The rectangle and rhombus enclosed by solid black lines denote the unit cells for  $\beta_{12}$  and  $\chi_3$  borophenes.

the Methods section for details). The EPC constants for  $\beta_{12}$  and  $\chi_3$  borophenes are 0.89 and 0.95, which can give rise to 18.7 K and 24.7 K superconductivity, respectively.

## II. METHODS

In our calculations the plane wave basis method was used [35]. We adopted the generalized gradient approximation (GGA) of Perdew-Burke-Ernzerhof [36] for the exchange-correlation potentials. The norm-conserving pseudopotentials [37] were used to model the electron-ion interactions. For the slab model, a vacuum layer with 15 Å in thickness was added to avoid the nonphysical coupling between adjacent boron sheets along the  $c$  axis. After a full convergence test, the kinetic energy cutoff and the charge density cutoff of the plane wave basis were chosen to be 60 Ry and 240 Ry, respectively. The self-consistent electron densities in  $\beta_{12}$  and  $\chi_3$  borophenes were evaluated on  $60 \times 40 \times 1$  and  $48 \times 48 \times 1$   $\mathbf{k}$ -point grids, respectively, combining with the Marzari-Vanderbilt smearing technique [38] of width 0.02 Ry. The lattice constants after full relaxation were adopted. The effect of electron doping was simulated by adding extra electrons. A compensating jellium background was introduced to avoid numerical divergence in a periodic calculation.

The dynamical matrices and phonon perturbation potentials [39] were calculated on a  $\Gamma$ -centered  $12 \times 8 \times 1$  mesh for  $\beta_{12}$  borophene and a  $12 \times 12 \times 1$  mesh for  $\chi_3$  borophene, within the framework of density-functional perturbation theory [40]. Maximally localized Wannier functions (MLWFs) [41] were determined on the same meshes of the Brillouin zone as that used in above phonon calculations. The random projection method, including nine (seven) Wannier functions, was used to construct MLWFs in  $\beta_{12}$  ( $\chi_3$ ) borophene. Eventually, fine electron (phonon) grids of  $960 \times 640 \times 1$  ( $240 \times 160 \times 1$ ) and  $720 \times 720 \times 1$  ( $180 \times 180 \times 1$ ) were used to interpolate the EPC quantities in  $\beta_{12}$  and  $\chi_3$  borophenes with the EPW code [42]. In  $\beta_{12}$  borophene, Dirac  $\delta$  functions for electrons and phonons are replaced by smearing functions with widths of 15 and 0.2 meV, respectively. These two quantities were selected

to be 35 and 0.2 meV in  $\chi_3$  borophene. The convergence test of EPC constant is given in Appendix A.

EPC was calculated based on Eliashberg equations [43]. The Eliashberg spectral function reads

$$\alpha^2 F(\omega) = \frac{1}{2\pi N(e_F)} \sum_{\mathbf{q}\nu} \delta(\omega - \omega_{\mathbf{q}\nu}) \frac{\gamma_{\mathbf{q}\nu}}{\hbar\omega_{\mathbf{q}\nu}}, \quad (1)$$

in which  $\omega_{\mathbf{q}\nu}$  and  $\gamma_{\mathbf{q}\nu}$  are the frequency and linewidth for phonon mode  $\nu$  at wave vector  $\mathbf{q}$ , and  $N(e_F)$  is the density of states at the Fermi level. The total EPC constant for the investigated compound can be determined by either Brillouin-zone summation or the frequency-space integration:

$$\lambda = \sum_{\mathbf{q}\nu} \lambda_{\mathbf{q}\nu} = 2 \int \frac{\alpha^2 F(\omega)}{\omega} d\omega, \quad (2)$$

where  $\lambda_{\mathbf{q}\nu}$  is the EPC constant for phonon mode  $\mathbf{q}\nu$ .

Using the McMillian-Allen-Dynes formula [44,45], we can evaluate the superconducting transition temperature as follows:

$$T_c = \frac{\omega_{\log}}{1.2} \exp \left[ \frac{-1.04(1 + \lambda)}{\lambda(1 - 0.62\mu^*) - \mu^*} \right], \quad (3)$$

where  $\mu^*$  is the effective screened Coulomb repulsion constant whose value is generally chosen to be between 0.1 and 0.15 [46,47], and  $\omega_{\log}$  is defined through

$$\omega_{\log} = \exp \left[ \frac{2}{\lambda} \int \frac{d\omega}{\omega} \alpha^2 F(\omega) \log \omega \right]. \quad (4)$$

## III. RESULTS

The structures of borophenes observed in experiment are schematically shown in Fig. 1. These two structures of borophenes are planar without out-of-plane buckling. Vacancy sites in them form rectangular and rhombic patterns. The vacancy concentration and coordination number are two quantities to describe the boron sheets from global and local points of view, respectively [14,19]. The vacancy concentration  $\eta$  is defined as the ratio between number of vacancy sites and total sites (including vacancy) in the unit cell. For example,  $\eta$  is equal to 1/6 in  $\beta_{12}$  borophene, and 1/5 in  $\chi_3$  borophene. The common values of coordination number for the 2D boron sheet are four, five, or six. The ratios among the above-mentioned three kinds of coordination atoms are 2:2:1 in  $\beta_{12}$  borophene, and 2:2:0 in  $\chi_3$  borophene. After structural optimization, the lattice constants along the  $a$  and  $c$  axes for  $\beta_{12}$  borophene are 2.9346 Å and 5.0840 Å, consistent with previous results [21]. In  $\chi_3$  borophene, the cell parameter is 4.4566 Å, with the acute angle in the rhombic cell being 38.207°.

First, we studied the electronic structures of  $\beta_{12}$  and  $\chi_3$  borophenes, using optimized crystal parameters. The calculated band structures and Fermi surfaces were given in Fig. 2. For both compounds, the band structures unambiguously manifest metallicity, in good agreement with significant density of states around the Fermi level measured by scanning tunneling spectroscopy [21]. In  $\beta_{12}$  borophene, there are three bands crossing the Fermi level. The first two bands contribute two elliptical hole Fermi sheets surrounding the zone center, as shown on right panel in Fig. 2(a). Dissimilarly, the third band forms two semielliptical electron-like Fermi sheets around

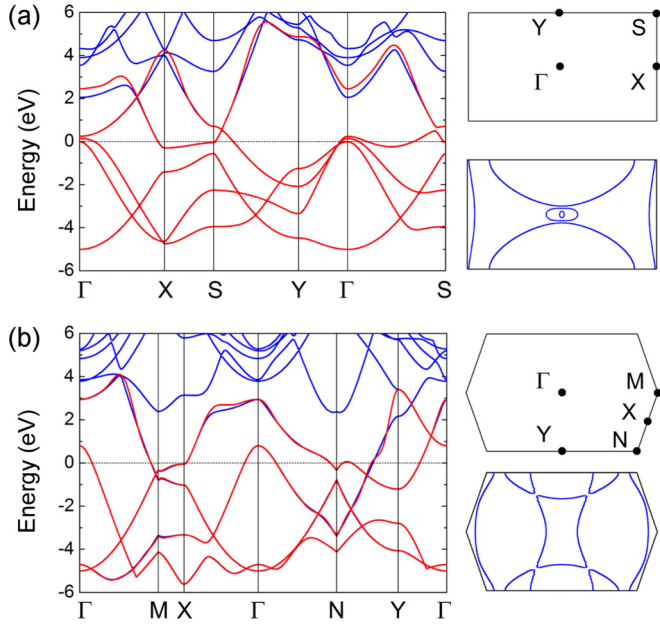


FIG. 2. Calculated electronic structures of  $\beta_{12}$  and  $\chi_3$  borophenes. (a) The band structure of  $\beta_{12}$  (left panel) and the Brillouin zone and Fermi surfaces (right panel). (b) The band structure of  $\chi_3$  (left panel) and the Brillouin zone and Fermi surfaces (right panel). The blue lines represent band structures given by first-principles calculation. The red curves are obtained by interpolation of maximally localized Wannier functions (MLWFs). The Fermi energy is set to zero. The high-symmetry points used in the band-structure calculations are labeled in the corresponding Brillouin zone.

the Brillouin zone boundary. For  $\chi_3$  borophene, we found that only two bands are partially occupied in the band structure [left panel of Fig. 2(b)]. The lower band in energy gives a twisted quadrilateral hole Fermi sheet around the  $\Gamma$  point. All other pieces of Fermi sheets in the Fermi surface plot [right panel of Fig. 2(b)] are electron Fermi sheets, originated from the second partially occupied band. The Wannier interpolated band structures show excellent agreement with these obtained by first-principles calculations below 2 eV. This forms a solid foundation for subsequent EPW calculation.

Second, to explore the possible superconductivity in borophene, we calculated the phonon spectra, Eliashberg spectral functions. The obtained results for  $\beta_{12}$  borophene are shown in Fig. 3. Almost all the phonon modes have positive frequencies, except for the transverse branch near the  $\Gamma$  point with maximum negative value being  $-1.75$  meV [Fig. 3(a)]. The main peak in phonon density of states (DOS)  $F(\omega)$  locates at about 50 meV [Fig. 3(b)], due to the dispersionless nature of phonon bands around this frequency. For EPC in  $\beta_{12}$  borophene, we found there are two  $A_g$  phonon modes at the  $\Gamma$  point, which have large coupling with electrons, and the linewidth of the lower  $A_g$  mode is larger. The vibrational patterns in real space for these two  $A_g$  phonon modes were schematically shown in Fig. 3(c) and 3(d), respectively. Both  $A_g$  phonon modes correspond to in-plane bond-stretching modes. It is also interesting that the movements of six-coordination atoms in the two  $A_g$  phonon modes are negligible. The Eliashberg spectral function  $\alpha^2F(\omega)$  is a central quantity,

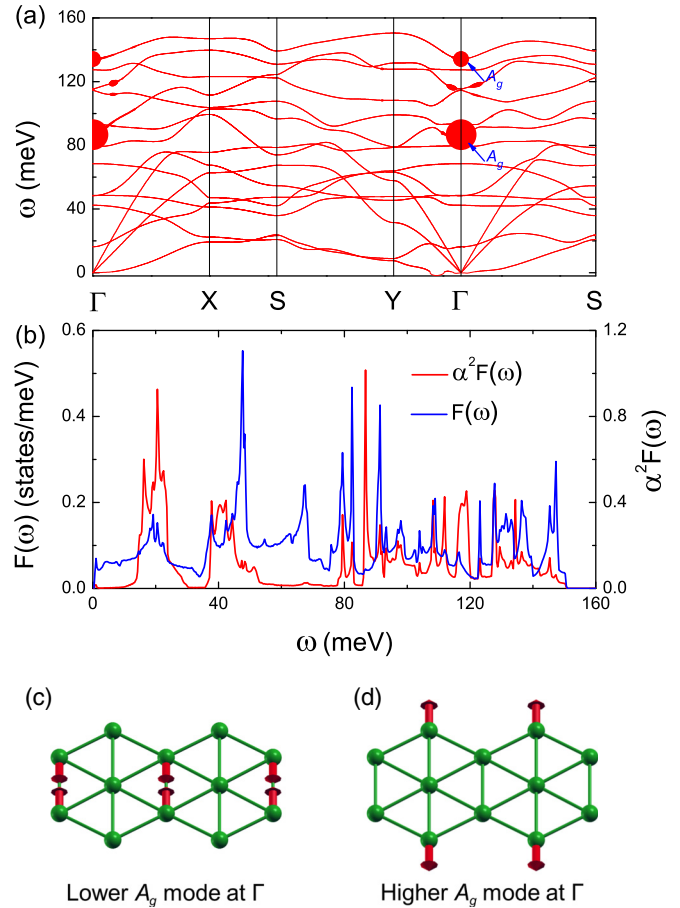


FIG. 3. Lattice dynamics of  $\beta_{12}$  borophene. (a) Phonon band structures, in which the linewidths for phonon mode  $\mathbf{q}\nu$  (i.e.,  $\gamma_{\mathbf{q}\nu}$ ) are represented by the widths of red lines. (b) Phonon density of states (DOS)  $F(\omega)$  and Eliashberg spectral function  $\alpha^2F(\omega)$ . (c) and (d) Vibrational pattern for two  $A_g$  phonon modes at  $\Gamma$ . The red arrows and their lengths denote the directions and relative amplitudes of these vibrational modes, respectively.

through which we can determine the EPC constant  $\lambda$  [Eq. (2)] and the logarithmic average frequency  $\omega_{\log}$  [Eq. (4)]. The sharp peak in  $\alpha^2F(\omega)$  around 87 meV resulted from the contribution of the lower  $A_g$  mode. In the calculation of  $\alpha^2F(\omega)$ ,  $\gamma_{\mathbf{q}\nu}$  is divided by the phonon frequency  $\omega_{\mathbf{q}\nu}$  [Eq. (1)]. And for  $\beta_{12}$  borophene, there exist certain low-frequency phonon modes whose  $\gamma_{\mathbf{q}\nu}/\omega_{\mathbf{q}\nu}$  is larger than that of the  $A_g$  mode. The emergence of a peak in Eliashberg spectral function around 20 meV is inevitable. We found  $\lambda = 0.89$ ,  $\omega_{\log} = 27.87$  meV, and  $T_c = 18.7$  K (setting  $\mu^*$  to 0.1) for  $\beta_{12}$  borophene.

The lattice dynamics and EPC properties of  $\chi_3$  borophene are presented in Fig. 4. Due to the translationally invariant symmetry, the frequencies of three acoustic phonons vanish at the  $\Gamma$  point, as they should [Fig. 4(a)]. A small negative phonon frequency of about  $-0.25$  meV was also found for the transverse phonon branch near the  $\Gamma$  point. There is a broadening peak in  $\alpha^2F(\omega)$ , extending from 15 meV to 40 meV [Fig. 4(b)]. The fine structures in this peak result from  $F(\omega)$ , due to the Dirac  $\delta$  function in Eq. (1). The Eliashberg spectral function resembles the phonon DOS above 40 meV. In  $\chi_3$  borophene, we identified four phonon modes

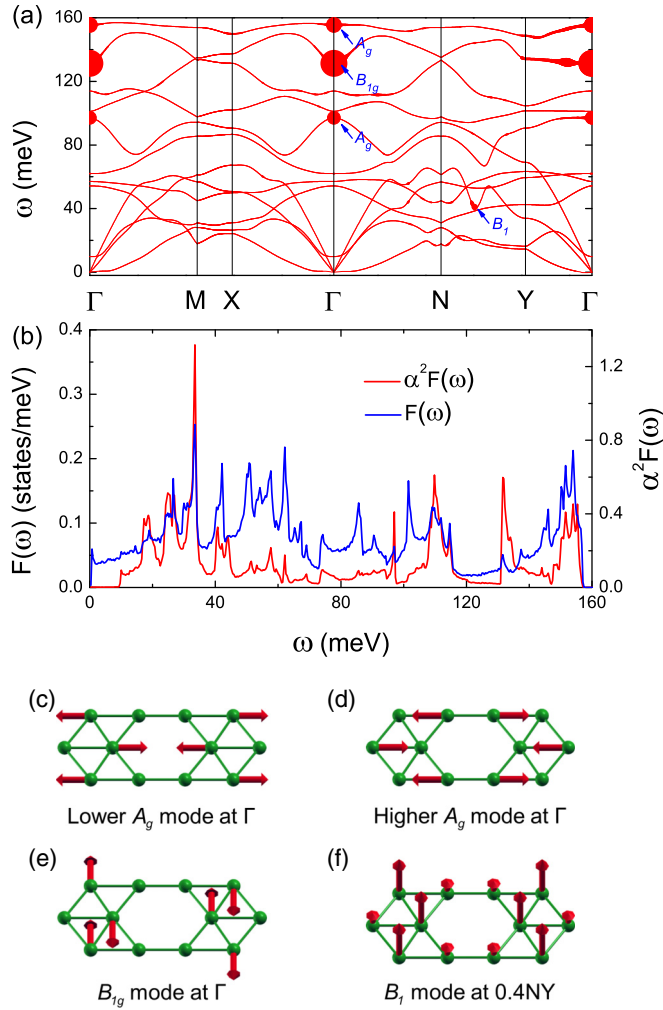


FIG. 4. Lattice dynamics of  $\chi_3$  borophene. (a) Phonon band structures, in which the linewidths for phonon mode  $\mathbf{q}\nu$  (i.e.,  $\gamma_{\mathbf{q}\nu}$ ) are represented by the widths of red lines. (b) Phonon DOS  $F(\omega)$  and Eliashberg spectral function  $\alpha^2 F(\omega)$ . (c)–(f) Vibrational patterns for important phonon modes. The red arrows and their lengths denote the directions and relative amplitudes of these vibrational modes, respectively.

with large EPCs. To be specific, they are the  $B_{1g}$  phonon mode, two  $A_g$  phonon modes at the  $\Gamma$  point, and the  $B_1$  phonon mode at about  $0.4NY$ . The above-mentioned zone-centered phonon modes involve the in-plane atomic movements, while the  $B_1$  mode corresponds to out-of-plane displacements of boron atoms. The  $B_{1g}$  phonon mode at  $\Gamma$  has the largest linewidth, which gives rise to a peak in  $\alpha^2 F(\omega)$  around 135 meV. Finally, the calculated  $\lambda$ ,  $\omega_{\log}$ , and  $T_c$  are 0.95, 33.10 meV, and 24.7 K, respectively. The EPC constant in  $\text{MgB}_2$  given by the Wannier interpolation technique is about 0.74 [48,49]. Thus both borophenes possess larger EPC constants in comparison with  $\text{MgB}_2$ .

The dynamical stability of a crystal structure is reflected by no imaginary phonon frequency in the Brillouin zone. But in both borophenes, our calculation showed that the frequency of the transverse branch becomes imaginary near the  $\Gamma$  point. For 2D compounds, two acoustical branches are linear with  $\mathbf{q}$  near the  $\Gamma$  point. On the contrary, due to the rapid

decay of force constants related to the transverse movements of atoms, the transverse branch always shows a quadratic dispersion near the  $\Gamma$  point [50]. The imaginary phonon frequency of the transverse branch near the  $\Gamma$  points was also found in the simulations of germanene [5], buckled arsenene [51], and other binary monolayer honeycomb structures [52]. The occurrence of imaginary frequency was attributed to the numerical difficulties in accurate calculation of rapid decaying interatomic forces, and is not a sign of structural transition [52]. Moreover, these imaginary frequencies do not affect our EPC results.

In order to have insight into the physical origin of strong coupling between electrons and the aforementioned phonons, we calculated differential charge densities (DCDs), i.e., charge density minus superposition of atomic charge densities, to determine the bonding nature in borophenes (see Fig. 5). For  $\beta_{12}$  borophene, the positive part of the DCD mostly distribute in the middle region of neighboring four-coordination and five-coordination boron atoms [Fig. 5(a)]. This unambiguously shows the formation of in-plane  $sp^2$ -hybridization-like  $\sigma$  bonds between these two kinds of boron atoms. The negative isosurface of the DCD is located on the top of each boron atom, resembling the  $B-2p_z$  orbital. Boron has three valance electrons. For an isolated boron atom, two electrons with opposite spin orientations will first occupy the  $B-2s$  orbital. Due to the degeneracy among  $B-2p_x$ ,  $B-2p_y$ , and  $B-2p_z$ , the third valance electron has the same probability to take one of the three orbitals. But in the borophene crystal, the energies of  $sp^2$ -hybridized orbitals are evidently lower than that of the  $B-2p_z$  orbital, the three valance electrons tend to fill the  $sp^2$ -hybridized bonding states, and as a result the occupation number in the  $B-2p_z$  orbital is significantly reduced. This is the reason for  $p_z$ -orbital-like negative DCD shown in Fig. 5(b). The  $B-2p_z$  orbital will overlap with its neighboring ones, forming  $\pi$  bands. The DCD and bonding characteristics in  $\chi_3$  borophene exhibit behavior similar to that in the  $\beta_{12}$  one [Figs. 5(e) and 5(f)].

We then projected the Kohn-Sham state  $\Psi_{nk}(r)$  to boron atomic orbitals. Figures 5(c) and 5(g) show the calculated orbital-resolved band structures for  $\beta_{12}$  and  $\chi_3$  borophenes, respectively. The widths of blue and green lines denote the contributions of  $2s + 2p_x + 2p_y$  and  $2p_z$  orbitals to given Kohn-Sham states. Detailed analysis shows that the uniform width of blue (green) lines is due to the fact that weights projected onto  $2s + 2p_x + 2p_y$  ( $2p_z$ ) are close to 1.0, suggesting that the blue (green) lines are pure  $\sigma$  ( $\pi$ ) bands. According to orbital-resolved band structures, we can further infer that the two hole Fermi sheets surrounding the  $\Gamma$  point in  $\beta_{12}$  borophene [Fig. 2(a)] are from  $\sigma$ -bonding bands. For  $\chi_3$  borophene, the top and bottom pieces of  $\Gamma$ -centered twisted quadrilateral Fermi sheets [Fig. 2(b)] stem from  $\pi$  bands;  $\sigma$ -bonding bands contribute to the left and right pieces. Meanwhile, the first Fermi sheet from the  $Y$  point to the  $N$  point in the Brillouin zone also belongs to  $\sigma$ -bonding bands.

Since the lower  $A_g$  phonon mode and the  $B_{1g}$  mode at  $\Gamma$  have the largest phonon linewidth in  $\beta_{12}$  and  $\chi_3$  borophenes, respectively, it is important to answer which bands or Fermi surfaces couple to  $A_g$  or  $B_{1g}$  phonons. A simple method to investigate EPC for a  $\Gamma$ -point optical phonon mode is to calculate the deformation potential caused by this phonon displacement

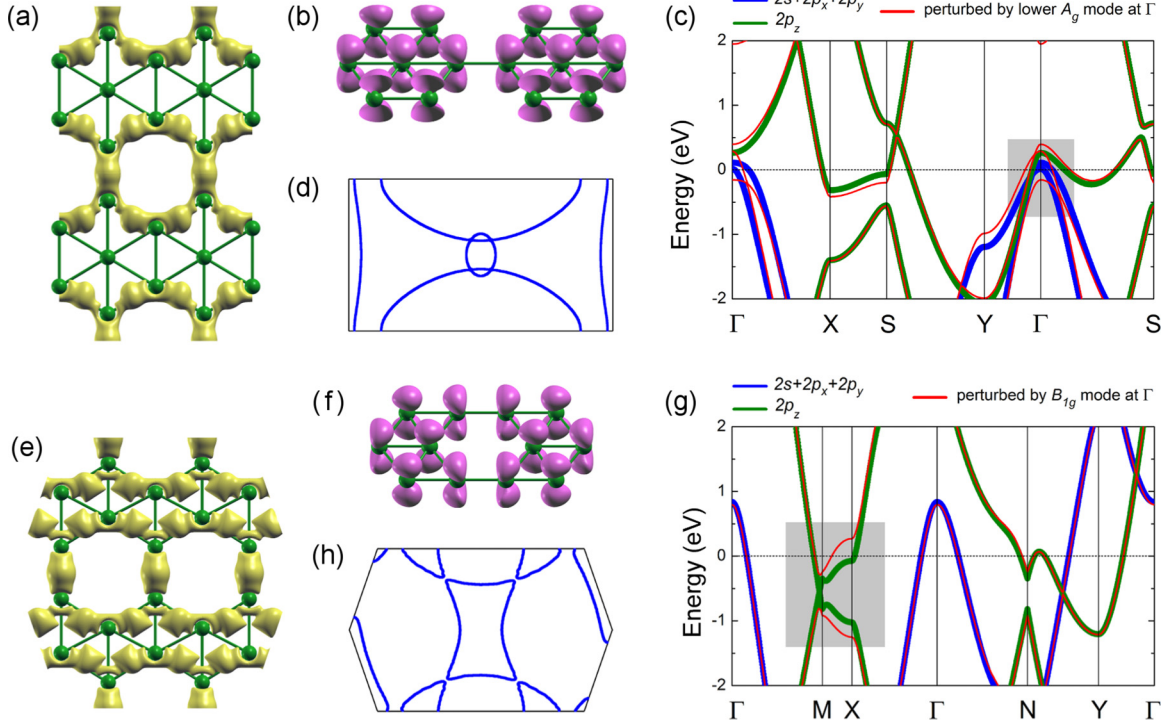


FIG. 5. Positive DCD (isovalue:  $2.8 \times 10^{-2} e/\text{bohr}^3$ ) (a), negative DCD (isovalue:  $-8.0 \times 10^{-3} e/\text{bohr}^3$ ) (b), orbital-resolved and phonon-perturbed band structures (c), and Fermi surfaces perturbed by  $B_{3g}$  phonon mode (d) in  $\beta_{12}$  borophene. Positive DCD (isovalue:  $2.45 \times 10^{-2} e/\text{bohr}^3$ ) (e), negative DCD (isovalue:  $-8.0 \times 10^{-3} e/\text{bohr}^3$ ) (f), orbital-resolved and phonon-perturbed band structures (g), and Fermi surfaces perturbed by  $B_{3g}$  phonon mode (h) in  $\chi_3$  borophene. The widths of blue and green lines in the band structures stand for the weights of  $2s + 2p_x + 2p_y$  and  $2p_z$  orbitals of boron in given Kohn-Sham state. The red lines represent the band structures perturbed by  $B_{3g}$  phonon modes at the  $\Gamma$  point. The obvious deviations in band structures before and after phonon perturbation are enclosed by gray shadows.

[53,54]. We moved the atomic positions according to the  $A_g$  or  $B_{1g}$  phonon displacement, and recalculated the band structures perturbed by phonons, namely the deformation potential. In the calculation of perturbed band structures and Fermi surfaces, the  $A_g$  and  $B_{1g}$  phonon displacements are normalized to 0.05 Å to obtain a clear vision. Figures 5(c) and 5(g) show the band structures before and after phonon perturbation. For  $\beta_{12}$  borophene, the  $\sigma$ -bonding bands near  $\Gamma$  are dramatically changed with respect to the equilibrium band structures [see gray shadow in Fig. 5(c)]. On the contrary, all the  $\pi$  bands are almost unaffected. The perturbed Fermi surfaces again confirm the above effects, with obvious distortions of the two  $\Gamma$ -centered hole Fermi sheets [Fig. 5(d)]. This means these two hole Fermi sheets, originated from  $\sigma$ -bonding bands, strongly couple to the  $A_g$  phonon in  $\beta_{12}$  borophene. For  $\chi_3$  borophene, the positions of the  $\pi$  band along the  $M$ - $X$  line are shifted after phonon perturbation [Fig. 5(g)], suggesting strong coupling between these bands and the  $B_{1g}$  phonon mode. As a consequence, the Fermi sheets near the lower right and top left corners considerably shrink [Fig. 5(h)].

#### IV. DISCUSSION

Among the theoretically proposed models for the boron sheet, neither  $\beta_{12}$  nor  $\chi_3$  is the ground-state structure [19]. Thus, the interfacial boron-silver interaction should play an important role in stabilizing these two monolayer structures on the Ag(111) substrate. Experiment indeed observed a charge

transfer from Ag(111) to the boron sheet [21]. The slab simulation identified a tiny charge transfer ( $\sim 0.03 e/\text{boron}$  atom) from the Ag substrate to borophene [21]. So borophenes are slightly electron doped. After deposition, the periodicity of borophene observed in experiment along the  $[\bar{1}\bar{1}2]$  direction of the Ag(111) surface is 15.0688 Å [21]. Due to lattice mismatch, this will impose 2.7% and 3.3% uniaxial tensile strains on  $\beta_{12}$  and  $\chi_3$  borophenes, respectively. For electron doping, our calculations showed the superconducting transition temperatures are slightly suppressed to 12.9 K and 21.6 K in these two compounds. After taking the tensile strains into consideration, the  $T_c$ s are further reduced by about 57% and 41% in  $\beta_{12}$  and  $\chi_3$  borophenes, with respect to the freestanding case (see Table I).

The strong EPC may raise the question of lattice instability. We found that the frequency of the lower  $A_g$  ( $B_{1g}$ ) phonon change from 87.4 (131.3) meV to 88.5 (118.4) meV in  $\beta_{12}$  ( $\chi_3$ ) borophene, by simulating the combined effects of charge transfer (0.03  $e/\text{boron}$ ) and tensile strain (2.7% in  $\beta_{12}$ , 3.3% in  $\chi_3$ ) provided by the Ag substrate. Thus no obvious phonon softening is found, when taking the substrate effect into consideration. Especially, the slightly hardened  $A_g$  phonon indicates that the substrate can further stabilize  $\beta_{12}$  borophene at the cost of degressive  $T_c$ . The strength of EPC is reserved to some extent in both borophenes, whose  $T_c$ s are still above the predicted 8.1 K superconductivity in graphene. On the other hand, the crystal structure of the deposited boron sheet strongly depends on the noble-metal substrate [24]. There is

TABLE I. Superconductivity in 2D compounds, including graphene [29], silicene [32], phosphorene [33], stanene [55], and borophene, predicted by first-principles calculations. Additional charge carriers were introduced by either deposition of guest atoms or electron doping. The strain is defined as  $\varepsilon = (a - a_0)/a_0 \times 100\%$ , in which  $a_0$  and  $a$  are the lattice constants of equilibrium and strained structures, respectively.

compounds	doping	$\varepsilon$ (%)	$\lambda$	$\omega_{\log}$ (meV)	$T_c$ (K)
graphene	Li deposition	0.0	0.61	34.44	8.1
silicene	0.44 $e$ /atom	0.0	0.44	29.38	1.7
	0.39 $e$ /atom	5.0	1.04	26.17	15.5
phosphorene	0.10 $e$ /atom	0.0	0.54	21.86	4.2
	0.10 $e$ /atom	8.0	1.31	10.64	12.2
stanene	Li deposition	0.0	0.65	5.25	1.3
$\beta_{12}$ borophene	0.0	0.0	0.89	27.87	18.7
	0.03 $e$ /atom	0.0	0.72	30.00	12.9
	0.03 $e$ /atom	2.7	0.55	39.69	8.0
$\chi_3$ borophene	0.0	0.0	0.95	33.10	24.7
	0.03 $e$ /atom	0.0	0.89	32.04	21.6
	0.03 $e$ /atom	3.3	0.66	41.09	14.5

a possibility of growing a novel 2D boron sheet whose  $T_c$  is higher than that currently investigated, by adopting a different substrate.

We have discussed the influences of tensile strain and electron doping on superconductivity in suspended borophenes, without including the Ag substrate in the calculation. But the screening effect of the Ag substrate is also very important. Herein, we constructed a minimal model of  $\chi_3$  borophene on Ag(111) to estimate the effect of Ag substrate. Considering the tremendous workload in EPC computing, we adopted a single silver atom layer to represent the Ag(111) surface. This model has a  $3 \times 3$ -Ag(111)-surface unit cell, in which there are 9 Ag atoms and 20 boron atoms. We labeled the above model as  $\chi_3$ /SL-Ag(111). The EPC of  $\chi_3$ /SL-Ag(111) was also calculated by the Wannier interpolation technique (see Appendix B for details). We found that  $T_c$  of  $\chi_3$ /SL-Ag(111) is 10.0 K, which is close to 14.5 K given in Table I. Although the  $T_c$  of  $\chi_3$  borophene is markedly reduced by Ag substrate, it is still higher than that found in superconducting graphene-based compounds.

Currently, several 2D compounds are predicted to be phonon-mediated superconductors in the literature by first-principles simulations. We listed the obtained quantities of these compounds in Table I to make a comparison. In the table, graphene, silicene, and stanene are Dirac semimetals, and phosphorene is a semiconductor. Additional charge carriers must be introduced to achieve superconductivity. For strain-free situation, the EPC constants of borophenes are the largest ones among the listed compounds. The  $T_c$  of 24.7 K in  $\chi_3$  borophenes is the highest one among these five 2D compounds without and with strain. After applying tensile strain, the superconducting transition temperatures of silicene and phosphorene increase to 15.5 K and 12.2 K, respectively. The influence of heavy electron/hole doping and/or large tensile/compressive strain on superconductivity in borophenes is also an important research subject, which needs to be clarified in further study.

In conclusion, we have studied the electronic structure and EPC in two kinds of borophene. The superconducting transition temperatures are around 20 K, which is higher than the observed 7.4 K superconductivity in graphene. Generally speaking, it is challenging for experiment to confirm superconductivity in 2D compounds on a conductive substrate. But very recently, four-point probe electrical transport measurements [56] and two-coil mutual inductance measurements [57] were successfully used to detect zero resistance and the Meissner effect, respectively, in monolayer FeSe film grown on Nb-doped SrTiO<sub>3</sub> substrate by molecular beam epitaxy. Here, Nb-doped SrTiO<sub>3</sub> is also a conductive substrate. Considering that borophene has been synthesized in experiment, our prediction can be directly examined by the above-mentioned two techniques.

*Note added.* Recently we noticed a paper by Penev *et al.* [58], who utilized the local density approximation and norm-conserving pseudopotentials to compute electron-phonon couplings in three structures of borophenes and drew similar conclusions.

## ACKNOWLEDGMENTS

This research is supported by the National Natural Science Foundation of China (Grants No. 11404383 and No. 11474004) and the Zhejiang Provincial Natural Science Foundation of China under Grant No. LY17A040005. This work is also sponsored by the K. C. Wong Magna Fund in Ningbo University.

## APPENDIX A: CONVERGENCE TEST OF ELECTRON-PHONON COUPLING CONSTANT

The correctness and accuracy of EPC calculation with the Wannier interpolation technique strongly rely on the spatial localization of the Hamiltonian ( $\|H(R)\|$ ) and dynamical matrix ( $\|D(R)\|$ ) in the Wannier representation. We have carefully examined the spatial decay of the above two quantities, which are shown in Fig. 6. The expressions of  $\|H(R)\|$  and  $\|D(R)\|$  read [39]

$$\begin{aligned} \|H(R)\| &= \max_{mn, \mathbf{R}_e - \mathbf{R}'_e = R} | \langle m \mathbf{R}'_e | \hat{H}^{el} | n \mathbf{R}_e \rangle |, \\ \|D(R)\| &= \max_{\kappa \kappa' \alpha \alpha', |\mathbf{R}_p - \mathbf{R}'_p| = R} | \langle \kappa' \alpha' \mathbf{R}_p | \hat{D}^{ph} | \kappa \alpha \mathbf{R}'_p \rangle |. \end{aligned}$$

$\hat{H}^{el}$  and  $\hat{D}^{ph}$  are the electron Hamiltonian and phonon dynamical matrix in the Bloch representation, respectively.  $m, n$  stand for the index of Wannier functions in one unit cell.  $\mathbf{R}_e, \mathbf{R}'_e, \mathbf{R}_p,$  and  $\mathbf{R}'_p$  represent the unit cell positions.  $\kappa$  and  $\kappa'$  denote the locations of atoms in one unit cell. Both  $\alpha$  and  $\alpha'$  traverse all three different directions of Cartesian coordinates.

The coarse  $\mathbf{k}$  meshes used in the determination of MLWFs were  $12 \times 8 \times 1$  and  $12 \times 12 \times 1$  for  $\beta_{12}$  and  $\chi_3$  borophenes. This means that the borophene crystals we computed are Wigner-Seitz supercells corresponding to  $12 \times 8 \times 1$  or  $12 \times 12 \times 1$  replicas of the primitive cell in periodic boundary simulation. The hopping distance among two MLWFs can extend to about 17 Å in both borophenes. While the hopping term of the Hamiltonian in the Wannier representation with distance outside the Wigner-Seitz supercell will be truncated in the generalized Fourier interpolation (see Eq. (31) in Ref. [39]). From Figs. 6(a) and 6(b), we found that the Hamiltonians

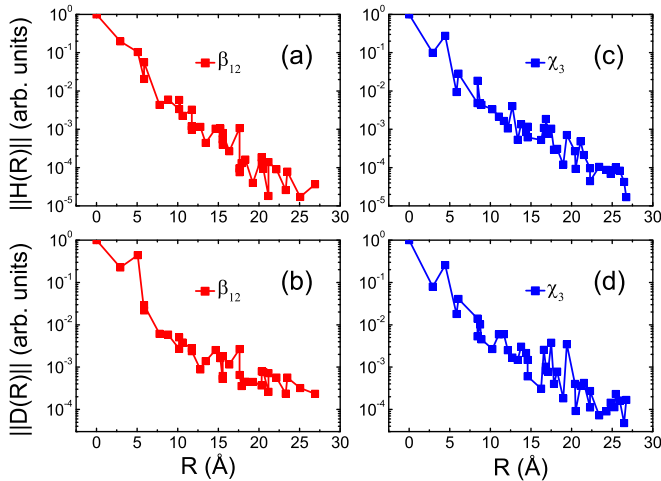


FIG. 6. Spatial decay of electronic Hamiltonian and dynamical matrix in the Wannier representation. (a) and (c) represented decay of electronic Hamiltonian for  $\beta_{12}$  and  $\chi_3$  borophene. Decay of dynamical matrix for  $\beta_{12}$  and  $\chi_3$  borophene are shown in (b) and (d), respectively.

in Wannier representation ( $\|H(R)\|$ ) show exponential decay with increasing  $R$ . Especially, the ratios between  $\|H(\sim 17 \text{ \AA})\|$  and  $\|H(0)\|$  decrease to  $1.07 \times 10^{-3}$  and  $7.60 \times 10^{-4}$  for  $\beta_{12}$  and  $\chi_3$  borophenes. The error in constructing the electron Hamiltonian for an arbitrary  $\mathbf{k}$  point introduced by Fourier interpolation is only 0.1%. On the other hand, the dynamical matrix in the Wannier representation is proportional to the interatomic force constants, whose spatial decay exhibits behavior similar to that for  $\|H(R)\|$  [see Figs. 6(c) and 6(d)]. Thus the electron Hamiltonian and phonon dynamical matrix in the Wannier representation constructed on the above used coarse  $\mathbf{k}$  and  $\mathbf{q}$  meshes are sufficient to interpolate EPC properties.

The difficulty in obtaining convergent  $\lambda$  originates from double  $\delta$  functions in calculating the EPC matrix element. In practical calculation, the  $\delta$  function is replaced by the smearing function with a broadening width  $\sigma$ . What we are interested in is the limit that  $\sigma \rightarrow 0$  and the number of  $\mathbf{k}$  points  $\rightarrow \infty$ . In order to obtain convergent  $\lambda$ , we have extensively tested the convergence versus  $\sigma$  and number of  $\mathbf{k}$  points, shown in Fig. 7 and Fig. 8. Although there is no plateau when  $\sigma$  is approaching zero in  $\beta_{12}$ , the fine meshes  $1200 \times 800 \times 1$  and  $960 \times 640 \times 1$  already give convergent  $\lambda$  for  $\sigma$  being 0.015 eV (see the inset in Fig. 7). Compared with commonly used  $0.01 \sim 0.02$  Ry for  $\sigma$  in the literatures, 0.015 eV is closer to the limit of  $\sigma \rightarrow 0$ . Thus we chose EPC properties obtained by  $\mathbf{k}$  mesh  $960 \times 640 \times 1$  and  $\sigma = 0.015$  eV as our results presented in the main text. For  $\chi_3$  borophene, the emergence of a small plateau near 0.035 eV and the overlapping results among different  $\mathbf{k}$  meshes at 0.035 eV clearly indicate that  $\lambda$  is convergent for  $720 \times 720 \times 1$  mesh and  $\sigma = 0.035$  eV.

The convergence of the  $\mathbf{q}$  mesh for Brillouin zone summation in Eq. (2) is also tested by enlarging the fine  $\mathbf{q}$  meshes to  $300 \times 200 \times 1$  and  $240 \times 240 \times 1$  for  $\beta_{12}$  and  $\chi_3$  borophenes, respectively. We found that the differences in  $\lambda$ s are merely  $2.50 \times 10^{-4}$  for  $\beta_{12}$  and  $5.89 \times 10^{-5}$  for  $\chi_3$ , with respect to that given in the main text. We also checked the convergence

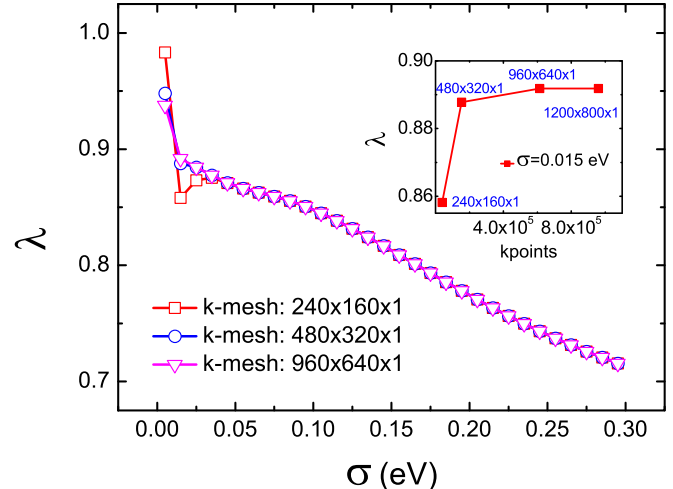


FIG. 7. Convergence test of EPC constant versus smearing parameter  $\sigma$  in  $\beta_{12}$  borophene. In the calculation, fine phonon grid was chosen to be  $240 \times 160 \times 1$ . The inset shows the convergence of  $\lambda$  for  $\sigma = 0.015$  eV, with increasing density of  $\mathbf{k}$  mesh.

of phonon frequency on the  $\mathbf{k}$  mesh that used to determine the self-consistent charge density. A smearing of 0.02 Ry together with a mesh of  $90 \times 60 \times 1$  yielded exactly the same frequencies for all the optical phonon modes at the  $\Gamma$  point for  $\beta_{12}$  borophene. A similar calculation was also carried out for  $\chi_3$  borophene by increasing the  $\mathbf{k}$  mesh from  $48 \times 48 \times 1$  to  $72 \times 72 \times 1$ . And we again did not observe any differences in the frequencies for optical phonon modes at  $\Gamma$ .

## APPENDIX B: EFFECT OF Ag SUBSTRATE

The  $\chi_3$ /SL-Ag(111) model contains one silver layer and one boron layer in the  $\chi_3$  configuration. Currently, we do not investigate  $\beta_{12}$ /SL-Ag(111) due to the huge number of atoms (105 atoms) in the  $3\sqrt{3} \times 5$ -Ag(111)-surface unit cell [21]. In the calculation of  $\chi_3$ /SL-Ag(111), a  $8 \times 8 \times 1$   $\mathbf{k}$  mesh together

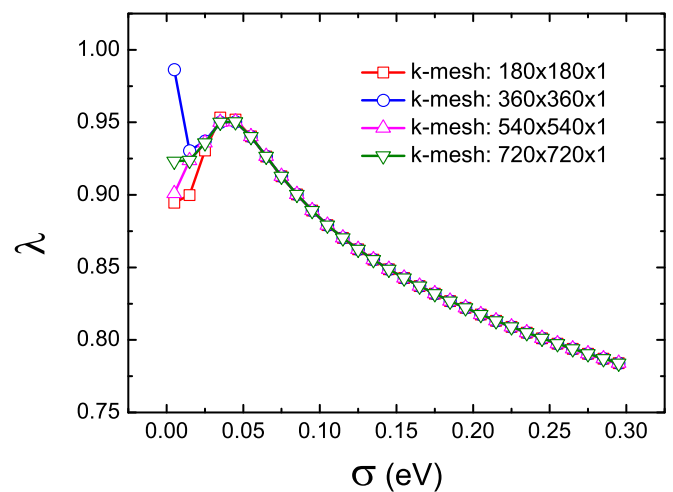


FIG. 8. Convergence test of EPC constant versus smearing parameter  $\sigma$  in  $\chi_3$  borophene. In the calculation, fine phonon grid was chosen to be  $180 \times 180 \times 1$ .

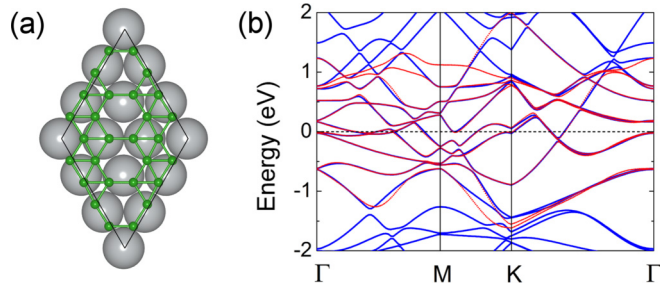


FIG. 9. (a) Ground-state structure of  $\chi_3$ /SL-Ag(111). The gray balls represent Ag atoms. The solid lines denote the unit cell. (b) Band structures of  $\chi_3$ /SL-Ag(111) obtained by first-principles calculation (blue lines) and interpolation of MLWFs (red lines).

with a 0.02 Ry Marzari-Vanderbilt smearing technique were used to evaluate the self-consistent charge density. The lattice constant was fixed to 8.7 Å, which is three times as large as that for Ag(111) surface. By relaxation of inner coordinates for silver and boron atoms, we obtained the ground-state structure of  $\chi_3$ /SL-Ag(111) [see Fig. 9(a)]. Here, we constructed ten MLWFs, with which the energy band at an arbitrary  $\mathbf{k}$  point can be interpolated. As can be seen in Fig. 9(b), the interpolated band structure is in excellent agreement with the one calculated by first principles from  $-0.5$  eV to  $0.5$  eV.

Dynamical matrices and phonon perturbation potentials were calculated on a coarse  $4 \times 4 \times 1$   $\mathbf{q}$  mesh. After the convergence test, the fine  $\mathbf{k}$  and  $\mathbf{q}$  mesh used in the EPW code were chosen to be  $240 \times 240 \times 1$  and  $80 \times 80 \times 1$ , respectively. In the phonon DOS (Fig. 10), the phonon

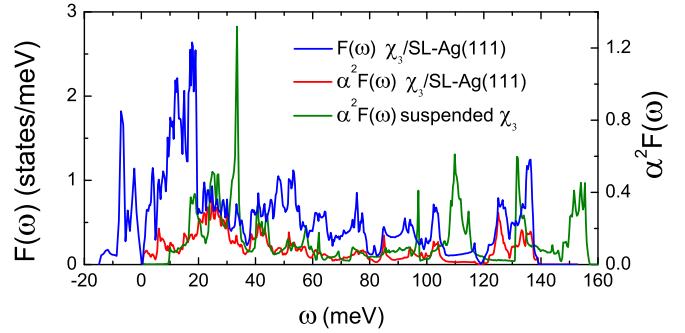


FIG. 10. Phonon DOS and Eliashberg spectral function for  $\chi_3$ /SL-Ag(111).

frequencies are significantly softened after including the Ag substrate. For example, the highest phonon frequency is reduced by about 12.5% with respect to that in suspended  $\chi_3$  borophene. We also found that there are some imaginary phonon frequencies, which may be related to the fact that only one single Ag layer is contained in  $\chi_3$ /SL-Ag(111). The Eliashberg spectral function  $\alpha^2 F(\omega)$  of  $\chi_3$ /SL-Ag(111) is redshifted in comparison with suspended  $\chi_3$  borophene (Fig. 10). According to Eq. (2) and Eq. (4), redshifted  $\alpha^2 F(\omega)$  will give rise to ascendent  $\lambda$  and descendent  $\omega_{\text{log}}$ . Finally, we found that  $\omega_{\text{log}} = 11.48$  meV,  $\lambda = 1.05$ , and  $T_c = 10.0$  K for  $\chi_3$ /SL-Ag(111). We also noticed the tensile strain and electron doping can also suppress superconductivity of  $\chi_3$  borophene through reducing  $\lambda$ . Thus, this indicates that the effect of the Ag substrate cannot be simply replaced by tensile strain and electron doping.

- [1] A. K. Geim and K. S. Novoselov, The rise of graphene, *Nat. Mater.* **6**, 183 (2007).
- [2] B. Aufray, A. Kara, S. Vizzini, H. Oughaddou, C. Léandri, B. Ealet, and G. Le Lay, Graphene-like silicon nanoribbons on Ag(110): A possible formation of silicene, *Appl. Phys. Lett.* **96**, 183102 (2010).
- [3] P. Vogt, P. De Padova, C. Quaresima, J. Avila, E. Frantzeskakis, M. C. Asensio, A. Resta, B. Ealet, and G. Le Lay, Silicene: Compelling Experimental Evidence for Graphenelike Two-Dimensional Silicon, *Phys. Rev. Lett.* **108**, 155501 (2012).
- [4] Yi Du, J. Zhuang, H. Liu, X. Xu, S. Eilers, K. Wu, P. Cheng, J. Zhao, X. Pi, K. W. See, G. Peleckis, X. Wang, and S. X. Dou, Tuning the band gap in silicene by oxidation, *ACS Nano* **8**, 10019 (2014).
- [5] S. Cahangirov, M. Topsakal, E. Aktürk, H. Şahin, and S. Ciraci, Two- and One-Dimensional Honeycomb Structures of Silicon and Germanium, *Phys. Rev. Lett.* **102**, 236804 (2009).
- [6] E. Bianco, S. Butler, S. Jiang, O. D. Restrepo, W. Windl, and J. E. Goldberger, Stability and exfoliation of germanane: A germanium graphane analogue, *ACS Nano* **7**, 4414 (2013).
- [7] M. Derivaz, D. Dentel, R. Stephan, M.-C. Hanf, A. Mehdaoui, P. Sonnet, and C. Pirri, Continuous germanene layer on Al(111), *Nano Lett.* **15**, 2510 (2015).
- [8] A. K. Geim and I. V. Grigorieva, Van der Waals heterostructures, *Nature (London)* **499**, 419 (2013).
- [9] Q. H. Wang, K. Kalantar-Zadeh, A. Kis, J. N. Coleman, and M. S. Strano, Electronics and optoelectronics of two-dimensional transition metal dichalcogenides, *Nat. Nanotechnol.* **7**, 699 (2012).
- [10] B. Radisavljevic, A. Radenovic, J. Brivio, V. Giacometti, and A. Kis, Single-layer MoS<sub>2</sub> transistors, *Nat. Nanotechnol.* **6**, 147 (2011).
- [11] S. Das, M. Demarteau, and A. Roelofs, Ambipolar phosphorene field effect transistor, *ACS Nano* **8**, 11730 (2014).
- [12] L. Li, Y. Yu, G. J. Ye, Q. Ge, X. Ou, H. Wu, D. Feng, X. H. Chen, and Y. Zhang, Black phosphorus field-effect transistors, *Nat. Nanotechnol.* **9**, 372 (2014).
- [13] J. Qiao, X. Kong, Z.-X. Hu, F. Yang, and W. Ji, High-mobility transport anisotropy and linear dichroism in few-layer black phosphorus, *Nat. Commun.* **5**, 4475 (2014).
- [14] H. Tang and S. Ismail-Beigi, Novel Precursors for Boron Nanotubes: The Competition of Two-Center and Three-Center Bonding in Boron Sheets, *Phys. Rev. Lett.* **99**, 115501 (2007).
- [15] X. Yang, Y. Ding, and J. Ni, *Ab initio* prediction of stable boron sheets and boron nanotubes: Structure, stability, and electronic properties, *Phys. Rev. B* **77**, 041402(R) (2008).
- [16] E. S. Penev, S. Bhowmick, A. Sadzadeh, and B. I. Yakobson, Polymorphism of two-dimensional boron, *Nano Lett.* **12**, 2441 (2012).

- [17] X. Yu, L. Li, X.-W. Xu, and C.-C. Tang, Prediction of two-dimensional boron sheets by particle swarm optimization algorithm, *J. Phys. Chem. C* **116**, 20075 (2012).
- [18] H. Tang and S. Ismail-Beigi, First-principles study of boron sheets and nanotubes, *Phys. Rev. B* **82**, 115412 (2010).
- [19] X. Wu, J. Dai, Y. Zhao, Z. Zhuo, J. Yang, and X. C. Zeng, Two-dimensional boron monolayer sheets, *ACS Nano* **6**, 7443 (2012).
- [20] A. J. Mannix *et al.*, Synthesis of borophenes: Anisotropic, two-dimensional boron polymorphs, *Science* **350**, 1513 (2015).
- [21] B. Feng *et al.*, Experimental realization of two-dimensional boron sheets, *Nat. Chem.* **8**, 563 (2016).
- [22] Y. Liu, E. S. Penev, and B. I. Yakobson, Probing the synthesis of two-dimensional boron by first-principles computations, *Angew. Chem., Int. Ed. Engl.* **52**, 3156 (2013).
- [23] B. Feng, J. Zhang, R.-Y. Liu, T. Iimori, C. Lian, H. Li, L. Chen, K. Wu, S. Meng, F. Komori, and I. Matsuda, Direct evidence of metallic bands in a monolayer boron sheet, *Phys. Rev. B* **94**, 041408(R) (2016).
- [24] Z. Zhang, Y. Yang, G. Gao, and B. I. Yakobson, Two-dimensional boron monolayers mediated by metal substrates, *Angew. Chem.* **127**, 13214 (2015).
- [25] S.-G. Xu, Y.-J. Zhao, J.-H. Liao, X.-B. Yang, and H. Xu, The nucleation and growth of borophene on the Ag (111) surface, *Nano Research* **9**, 2616 (2016).
- [26] S. De Franceschi, L. Kouwenhoven, Ch. Schönenberger, and W. Wernsdorfer, Hybrid superconductor-quantum dot devices, *Nat. Nanotechnol.* **5**, 703 (2010).
- [27] M. Huefner, C. May, S. Kižin, K. Ensslin, T. Ihn, M. Hilke, K. Suter, N. F. de Rooij, and U. Staufer, Scanning gate microscopy measurements on a superconducting single-electron transistor, *Phys. Rev. B* **79**, 134530 (2009).
- [28] B. Uchoa and A. H. Castro Neto, Superconducting States of Pure and Doped Graphene, *Phys. Rev. Lett.* **98**, 146801 (2007).
- [29] G. Profeta, M. Calandra, and F. Mauri, Phonon-mediated superconductivity in graphene by lithium deposition, *Nat. Phys.* **8**, 131 (2012).
- [30] A. P. Tiwari, S. Shin, E. Hwang, S.-G. Jung, T. Park, and H. Lee, Superconductivity at 7.4 K in few layer graphene by Li intercalation, [arXiv:1508.06360](https://arxiv.org/abs/1508.06360).
- [31] J. Chapman, Y. Su, C. A. Howard, D. Kundys, A. Grigorenko, F. Guinea, A. K. Geim, I. V. Grigorieva, and R. R. Nair, Superconductivity in Ca-doped graphene laminates, *Sci. Rep.* **6**, 23254 (2016).
- [32] W. Wan, Y. Ge, F. Yang, and Y. Yao, Phonon-mediated superconductivity in silicene predicted by first-principles density functional calculations, *Europhys. Lett.* **104**, 36001 (2013).
- [33] D. F. Shao, W. J. Lu, H. Y. Lv, and Y. P. Sun, Electron-doped phosphorene: A potential monolayer superconductor, *Europhys. Lett.* **108**, 67004 (2014).
- [34] Y. Ge, W. Wan, F. Yang, and Y. Yao, The strain effect on superconductivity in phosphorene: A first principles prediction, *New J. Phys.* **17**, 035008 (2015).
- [35] P. Giannozzi *et al.*, QUANTUM ESPRESSO: A modular and open-source software project for quantum simulations of materials, *J. Phys.: Condens. Matter* **21**, 395502 (2009).
- [36] J. P. Perdew, K. Burke, and M. Ernzerhof, Generalized Gradient Approximation Made Simple, *Phys. Rev. Lett.* **77**, 3865 (1996).
- [37] N. Troullier and J. L. Martins, Efficient pseudopotentials for plane-wave calculations, *Phys. Rev. B* **43**, 1993 (1991).
- [38] N. Marzari, D. Vanderbilt, A. De Vita, and M. C. Payne, Thermal Contraction and Disordering of the Al(110) Surface, *Phys. Rev. Lett.* **82**, 3296 (1999).
- [39] F. Giustino, M. L. Cohen, and S. G. Louie, Electron-phonon interaction using Wannier functions, *Phys. Rev. B* **76**, 165108 (2007).
- [40] S. Baroni, S. de Gironcoli, A. Dal Corso, and P. Giannozzi, Phonons and related crystal properties from density-functional perturbation theory, *Rev. Mod. Phys.* **73**, 515 (2001).
- [41] A. A. Mostofi *et al.*, wannier90: A tool for obtaining maximally-localised Wannier functions, *Comput. Phys. Commun.* **178**, 685 (2008).
- [42] J. Noffsinger *et al.*, EPW: A program for calculating the electron-phonon coupling using maximally localized Wannier functions, *Comput. Phys. Commun.* **181**, 2140 (2010).
- [43] G. M. Eliashberg, Interactions between electrons and lattice vibrations in a superconductor, *Sov. Phys. JETP* **11**, 696 (1960).
- [44] P. B. Allen, Neutron spectroscopy of superconductors, *Phys. Rev. B* **6**, 2577 (1972).
- [45] P. B. Allen and R. C. Dynes, Transition temperature of strong-coupled superconductors reanalyzed, *Phys. Rev. B* **12**, 905 (1975).
- [46] C. F. Richardson and N. W. Ashcroft, High-Temperature Superconductivity in Metallic Hydrogen: Electron-Electron Enhancements, *Phys. Rev. Lett.* **78**, 118 (1997).
- [47] K.-H. Lee, K. J. Chang, and M. L. Cohen, First-principles calculations of the Coulomb pseudopotential  $\mu^*$ : Application to Al, *Phys. Rev. B* **52**, 1425 (1995).
- [48] M. Calandra, G. Profeta, and F. Mauri, Adiabatic and nonadiabatic phonon dispersion in a Wannier function approach, *Phys. Rev. B* **82**, 165111 (2010).
- [49] E. R. Margine and F. Giustino, Anisotropic Migdal-Eliashberg theory using Wannier functions, *Phys. Rev. B* **87**, 024505 (2013).
- [50] F. Liu, P. Ming, and J. Li, *Ab initio* calculation of ideal strength and phonon instability of graphene under tension, *Phys. Rev. B* **76**, 064120 (2007).
- [51] C. Kamal and M. Ezawa, Arsenene: Two-dimensional buckled and puckered honeycomb arsenic systems, *Phys. Rev. B* **91**, 085423 (2015).
- [52] H. Şahin, S. Cahangirov, M. Topsakal, E. Bekaroglu, E. Akturk, R. T. Senger, and S. Ciraci, Monolayer honeycomb structures of group-IV elements and III-V binary compounds: First-principles calculations, *Phys. Rev. B* **80**, 155453 (2009).
- [53] F. S. Khan and P. B. Allen, Deformation potentials and electron-phonon scattering: Two new theorems, *Phys. Rev. B* **29**, 3341 (1984).
- [54] J. M. An and W. E. Pickett, Superconductivity of MgB<sub>2</sub>: Covalent Bonds Driven Metallic, *Phys. Rev. Lett.* **86**, 4366 (2001).
- [55] Y. Shaidu and O. Akin-Ojo, First principles predictions of superconductivity in doped stanene, [arXiv:1506.07114](https://arxiv.org/abs/1506.07114).
- [56] J.-F. Ge *et al.*, Superconductivity above 100 K in single-layer FeSe films on doped SrTiO<sub>3</sub>, *Nat. Mater.* **14**, 285 (2015).
- [57] Z. Zhang *et al.*, Onset of the Meissner effect at 65 K in FeSe thin film grown on Nb-doped SrTiO<sub>3</sub> substrate, *Sci. Bull.* **60**, 1301 (2015).
- [58] E. S. Penev, A. Kutana, and B. I. Yakobson, Can two-dimensional boron superconduct?, *Nano Lett.* **16**, 2522 (2016).